GLOBAL INVENTORY AND CHARACTERIZATION OF PYROCLASTIC DEPOSITS ON MERCURY: NEW INSIGHTS INTO PYROCLASTIC ACTIVITY FROM MESSENGER ORBITAL DATA. Timothy A. Goudge[1], James W. Head[1], Laura Kerber[2], David T. Blewett[3], Brett W. Denevi[3], Scott L. Murchie[3], Noam R. Izenberg[3], William E. McClintock[4], Gregory M. Holsclaw[4], Deborah L. Domingue[5], Jeffrey J. Gillis-Davis[6], Zhiyong Xiao[7], Robert G. Strom[7], Jörn Helbert[8], and Sean C. Solomon[9]. [1]Department of Geological Sciences, Brown University, Providence, RI 02912; [2]Laboratoire de Météorologie Dynamique, CNRS/UPMC/IPSL, 75252 Paris Cedex 05, France; [3]The Johns Hopkins University Applied Physics Laboratory, Laurel, MD 20723; [4]Laboratory for Atmospheric and Space Physics, University of Colorado, Boulder, CO 80303; [5]Planetary Science Institute, Tucson, AZ 85719; [6]Hawai'i Institute of Geophysics and Planetology, University of Hawai'i, Honolulu, HI 96822; [7]Lunar and Planetary Laboratory, University of Arizona, Tucson, AZ 85719; [8]DLR, Rutherfordstrasse 2, Berlin, Germany; [9]Department of Terrestrial Magnetism, Carnegie Institution of Washington, Washington, DC 20015 (Contact: Tim_Goudge@brown.edu).

Introduction: From data acquired during the three flybys of Mercury by the MErcury Surface, Space ENvironment, GEochemistry, and Ranging (MESSENGER) spacecraft [1], a number of sites were identified as pyroclastic deposits formed through explosive volcanic processes [2-8]. These deposits are of great interest, as they provide insight into the presence, composition, and nature of volatiles in the interior of Mercury. Here we present new observations on these and other pyroclastic deposits using data acquired following insertion of MESSENGER into orbit around Mercury.

Datasets and Methods: Morphologies of the pyroclastic deposits were investigated using high-resolution images from the Mercury Dual Imaging System (MDIS) narrow-angle camera (NAC) and wide-angle camera (WAC) [9]. Compositions of the pyroclastic deposits were investigated using MDIS 8-filter color images [9] and point spectra from the Mercury Atmospheric and Surface Composition Spectrometer (MASCS) instrument [10]. All utilized MDIS color images were photometrically corrected using the Hapke model [11], and MASCS spectra were corrected to reflectance using a simple geometric correction along with a phase term.

Update to the Global Pyroclastic Catalogue: In order to build upon the most recent global pyroclastic catalogue [8], all acquired MDIS NAC and WAC images were examined for rimless depressions [12] that could be source vents for pyroclastic deposits [7,8]. These candidate vents were then examined using MDIS color images to determine the presence of any associated red color and high-albedo anomaly, as are observed for previously identified pyroclastic deposits [2-8]. Of 13 initially identified rimless depressions, nine show associated color and albedo anomalies (Fig. 1, 2), indicating that these nine rimless depressions are likely to be vents associated with pyroclastic deposits (e.g., Fig. 2A). These newly identified vents are all associated with the floors, central peaks, peak rings, or rims of impact craters, consistent with the setting of previously identified deposits [8].

As with previously identified pyroclastic deposits [2-8], the nine new sites have a red spectral slope, higher albedo than surrounding terrain, and no absorption at 1000 nm as seen in spectral data from both the MDIS and MASCS instruments. The presence of a 1000 nm absorption would be indicative of a crystal-field effect caused by Fe^{2+} in a silicate mineral [13]. Its absence is consistent with both previous work [2-8] and XRS data that indicate a relatively Fe-poor crust [14].

One observation of interest is a pair of pits at northern high-latitudes [15], neither of which has an associated spectral anomaly (Fig. 2B). These pits are located just outside the northern volcanic smooth plains [15], and the lack of a distinctive spectral signature associated with these pits is consistent with the idea that more effusive volcanism can also create rimless depressions on the surface of Mercury [12,15].

Results of New Orbital Observations: Here we briefly summarize some of the new orbital data for three pyroclastic deposits [8]: NE Derzhavin and Praxiteles NE and SW.

NE Derzhavin: New NAC images of the NE Derzhavin deposit [8] (Fig. 3) show the vent of this deposit in great detail. The scarps of this vent in the northeastern (NE) corner are more well defined than in the western portion of the vent (Fig. 3A), suggesting multiple stages of evolution of the vent structure, either primary, or related to later slumping of the walls of the ~25-km-wide pit. This observation is supplemented by MDIS color data over the vent (Fig. 3B), which show an area of enhanced spectral contrast surrounding the NE portion of the vent. This enhanced spectral contrast could also suggest different ages and therefore different eruptive events or conditions. As part of our global characterization, we are examining each of the pyroclastic deposits in detail to look for additional evidence of variations in internal deposits.

Praxiteles NE and SW: The Praxiteles impact crater contains two pyroclastic deposits, one in the NE portion of the basin and one in the southwest (SW) [8] (Fig. 4A). One important question in characterizing these pyroclastic deposits is their relative ages and where they fall in the regional stratigraphy. In this example, it is clear that the SW vent is crosscut by a secondary crater chain (Fig. 4A, black arrows), traceable back to the ~114-km-diameter Hokusai crater. This indicates that pyroclastic activity at this site must have occurred prior to the formation of this large, rayed crater. We are searching for similar age relationships at other pyroclastic deposits.

MASCS spectra from the two Praxiteles pyroclastic deposits show both the characteristic red slope [2-8], as well as a slight downturn at shorter wavelengths (<400 nm) (Fig. 4B). This downturn is likely the edge of an oxygen-metal charge-transfer (OMCT) band, centered closer to ~250-280 nm, that is due to small amounts of Fe (or Ti) within the deposits [16], as has been suggested generally for Mercury's surface [17]. The relative weakness of this band and the lack of an absorption at 1000 nm indicates that the amount of Fe/Ti present is likely to be on the order of only a few wt. % [16,17]; however, Ti^{4+} can also cause such an OMCT band without producing a 1000 nm absorption [13,16]. The presence of this short-wavelength downturn in ratioed MASCS data (Fig. 4B) may indicate a slightly higher Fe/Ti content in the pyroclastic deposits than in the crater floor materials, although further analysis of MASCS data, along with the use of other instruments (e.g., XRS, which has a maximum resolution of ~40 km/pixel [18]), will be necessary to fully constrain the composition of these deposits.

In addition to the insights into timing and composition that are offered by the Praxiteles pyroclastic deposits, there is also

an association with the enigmatic hollows observed across the surface of Mercury [19] (Fig. 4A inset, orange arrows). Hollows can be seen both on the terrain surrounding the Praxiteles NE pyroclastic vent and on the walls of the vent itself (Fig. 4A inset, orange arrows). This relation indicates that the hollows at this site are younger than the pyroclastic activity, consistent with the hypothesis that hollows are relatively young features on the surface of Mercury [19]. A major question we are addressing in our characterization is whether there is some genetic association between hollows and pyroclastic deposits, both of which are thought to be related to volatiles [2-8, 19]. In addition to Praxiteles NE, hollows appear associated with three other pyroclastic deposits in published catalogues [8] (Lermontov SW, RS-03 SE, and RS-05) as well as within the crater Tyagaraja, as discussed earlier [19]. Such examples are being mapped in detail to address this question.

Conclusion: Orbital data of pyroclastic deposits have shown more detailed aspects of vent morphologies, relative ages, compositions, and geologic associations than previous studies with flyby data [2-8]. This global analysis of pyroclastic deposits on Mercury is ongoing, and future work will continue to address these aspects of pyroclastic activity on Mercury in an attempt to help understand both the composition and volatile content of Mercury's interior.

Acknowledgements: Special thanks are extended to D. Baker, M. Beach, D. Hurwitz, L. Jozwiak, K. Scanlon, W. Vaughn, and J. Whitten for assistance with the identification of possible pyroclastic vents.

References: [1] S.C. Solomon *et al.* (2008) *Science*. **321**:59. [2] J.W. Head *et al.* (2008) *Science*. **321**:69. [3] S.L. Murchie *et al.* (2008) *Science*. **321**:73. [4] M.S. Robinson *et al.* (2008) *Science*. **321**:66. [5] D.T. Blewett *et al.* (2009) *EPSL*. **285**:263. [6] J.W. Head *et al.* (2009) *EPSL*. **285**:227. [7] L. Kerber *et al.* (2009) *EPSL*. **285**:263. [8] L. Kerber *et al.* (2011) *PSS*. **59**:1895. [9] S.E. Hawkins, III, *et al.* (2007). *Space Sci. Rev.* **131**:247. [10] W.E. McClintock and M.R. Lankton (2007) *Space Sci. Rev.* **131**:481. [11] D.L. Domingue *et al.* (2010) *Icarus*. **209**:101. [12] J.J. Gillis-Davis *et al.* (2009) *EPSL*. **285**:243. [13] R.G. Burns (1970) *Mineralogic Applications of Crystal Field Theory*. Cambridge. [14] L.R. Nittler *et al.* (2011) *Science*. **333**:1847. [15] J.W. Head *et al.* (2011) *Science*. **333**:1853. [16] R.G. Burns (1993), in *Remote Geochemical Analysis*: *Elemental and Mineralogical Composition* (C. M. Pieters and P.A.J. Englert, Eds.). Cambridge. pp. 3-29. [17] W.E. McClintock *et al.* (2008) *Science*. **321**:62. [18] C.E. Schlemm, II, *et al.* (2007) *Space Sci. Rev.* **131**:393. [19] D.T. Blewett *et al.*(2011) *Science*. **333**:1856.

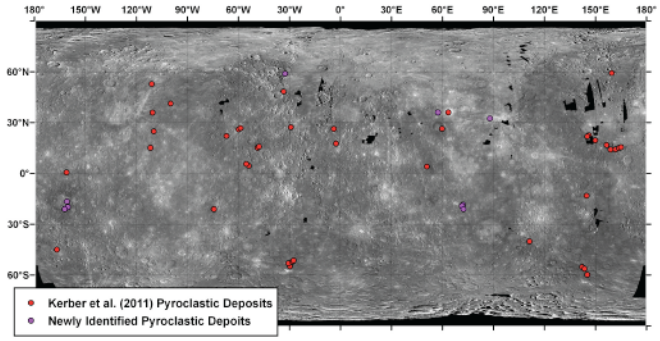

Figure 1: Locations of the 40 previously identified pyroclastic deposits [8] (red), as well as the nine pyroclastic deposits newly identified here (purple). Background is MDIS-derived NAC and WAC mosaic at 250 m/pixel (mpp).

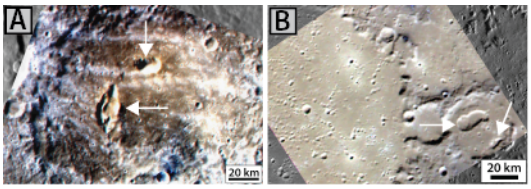

Figure 2: (A) Two newly identified pyroclastic deposits (white arrows) at 18.5ºS, and 71.5ºE. False-color image is from MDIS WAC 8-band color (R=996.8 nm, G=749 nm and B=430 nm) and images EW0221845266I-EW0221845294L overlain on MDIS-derived NAC and WAC 250 mpp global mosaic. **(B)** Two northern plains vents [15] (white arrows) at 59.4ºN, and 106.6ºE with no color or albedo anomaly. False-color image is from MDIS WAC 8-band color (R=996.8 nm, G=749 nm and B=430 nm) and images EW0218969013I- EW0218969025L overlain on MDIS-derived NAC and WAC 250 mpp global mosaic.

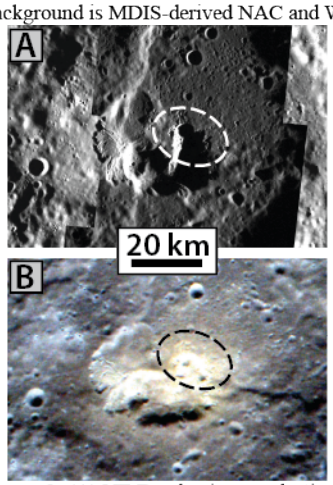

Figure 3: (A) NE Derzhavin pyroclastic deposit [8] at 48.4ºN, and 326.3ºE. Dashed line indicates sharply defined vent scarps. Image is MDIS NAC images EN0221237588M, EN0221237609M, and EN0221237630M overlain on MDIS-derived 250 mpp global mosaic. **(B)** Color image of NE Derzhavin. Dashed line indicates area of enhanced spectral contrast. False-color image is from MDIS WAC 8-band color (R=996.8 nm, G=749 nm and B=430 nm) and images EW0210764469I-EW0210764481L.

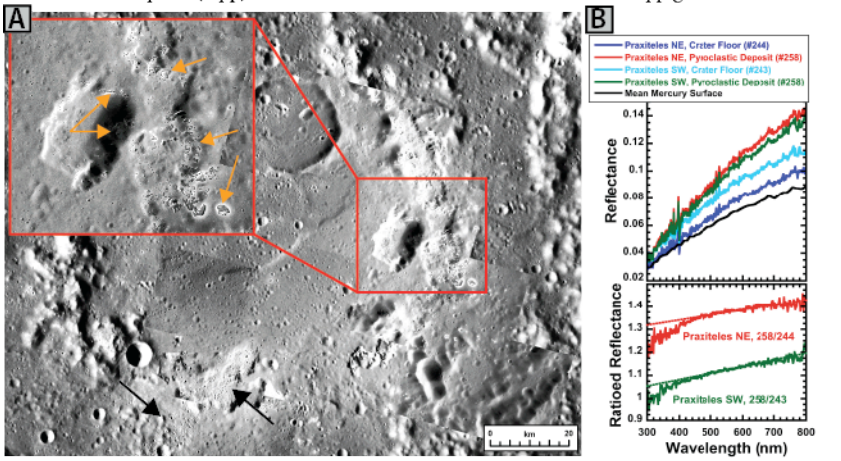

Figure 4: (A) Praxiteles crater at 27.3ºN, and 300.8ºE, containing two pyroclastic deposits, Praxiteles NE and Praxiteles SW [8] (north is up). Black arrows indicate a secondary crater chain from Hokusai crater that crosscuts the Praxiteles SW vent. Inset shows hollows surrounding the Praxiteles NE vent (orange arrows) [19]. Hollows also crosscut the vent walls. Image is MDIS NAC images EN0223831431M, EN0223831439M, EN0223831447M, and EN0223831455M (Praxiteles NE) and EN0223745067M, EN0223745074M, and EN0223745081M (Praxiteles SW) overlain on MDIS-derived 250 mpp global mosaic. **(B)** MASCS spectra from Praxiteles crater floor and pyroclastic deposits. Top panel shows geometrically corrected reflectance spectra. Spectra for Praxiteles NE are from MASCS track ORB_11106_043345, and spectra from Praxiteles SW are from MASCS track ORB_11105_163009. Spectra numbers along track are indicated in brackets in the legend. Lower panel shows ratioed reflectance spectra. Dashed lines are approximate linear continua. Note deviations from the continuum shortward of ~400 nm.